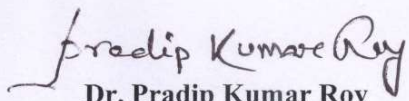


CERTIFICATE

It is certified that the work contained in the thesis titled "*Synthesis and characterizations of modified Y-type hexaferrite materials for potential applications in various fields*" by "**Mukesh Suthar**" has been carried out under our joint supervision, and this work has not been submitted elsewhere for a degree.

It is further certified that the student has fulfilled all the requirements of Comprehensive Examination, Candidacy, and SOTA for the award of a Ph.D. degree.

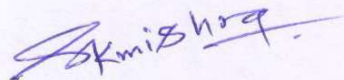


Dr. Pradip Kumar Roy

(Supervisor)

Associate Professor,
Department of Ceramic Engineering,
Indian Institute of Technology (BHU),
Banaras Hindu University,
Varanasi – 221005, (U.P.), India

Dr. Pradip Kumar Roy
Associate Professor
Department of Ceramic Engineering,
Indian Institute of Technology (I.I.T) (BHU),
Banaras Hindu University, Varanasi-221005
Uttar Pradesh (U.P.), INDIA



Dr. Shrawan Kumar Mishra

(Co-Supervisor)

Assistant Professor,
School of Material Science and Technology,
Indian Institute of Technology (BHU),
Banaras Hindu University,
Varanasi – 221005, (U.P.), India

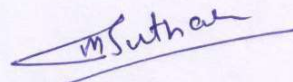
Dr. Shrawan Kumar Mishra
Assistant Professor
School of Materials Science & Technology
IIT (BHU), Varanasi-221005, INDIA

DECLARATION BY THE CANDIDATE

I, **Mukesh Suthar**, am certified that the work embodied in this Ph.D. thesis is my own bonafide work and carried out by me under the joint supervision of **Dr. P. K. Roy** and **Dr. S. K. Mishra** for a period from **July 2016** to **July 2022** at the “**Department of Ceramic Engineering**”, Indian Institute of Technology (BHU), Varanasi, India. The matter embodied in this Ph.D. thesis has not been submitted for the award of any other degree/diploma. I declare that I have faithfully acknowledged and given credits to the research workers wherever their works have been cited in my work in this thesis. I further declare that I have not willfully copied any other's work, paragraphs, text, data, results, etc., reported in journals, books, magazines, reports, dissertations, thesis, etc., or available on websites and have not included them in this thesis and have not cited as my own work.

Date : 11th July 2022

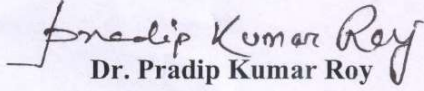
Place : Varanasi



(Mukesh Suthar)

CERTIFICATE BY THE SUPERVISORS

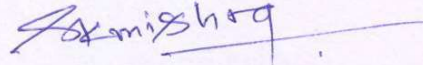
This is to certify that the above statement made by the candidate is correct to the best of our knowledge.


Dr. Pradip Kumar Roy

(Supervisor)

Associate Professor,

Department of Ceramic Engineering,
Indian Institute of Technology (BHU),
Banaras Hindu University,
Varanasi – 221005, (U.P.), India



Dr. Shrawan Kumar Mishra

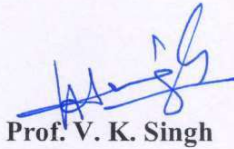
(Co-Supervisor)

Assistant Professor,

School of Material Science and Technology,
Indian Institute of Technology (BHU),
Banaras Hindu University,
Varanasi – 221005, (U.P.), India

Forwarded

by


Prof. V. K. Singh

(Head of the Department),

Department of Ceramic Engineering,
Indian Institute of Technology (BHU),
Banaras Hindu University,
Varanasi – 221005, (U.P.), India

HEAD/ विभागाध्यक्ष

Department of Ceramic Engineering

सिरामिक अभियान्त्रिकी विभाग
Indian Institute of Technology (I.I.T.)

भारतीय प्रौद्योगिकी संस्थान (का०हि०वि०वि०)

Varanasi-221005/ वाराणसी-221005

COPYRIGHT TRANSFER CERTIFICATE

Title of the Thesis: *Synthesis and Characterizations of Modified Y-Type Hexaferrite Materials for Potential Applications in Various Fields.*

Candidate's Name: *Mukesh Suthar*

COPYRIGHT TRANSFER

The undersigned hereby assigns to the Indian Institute of Technology (Banaras Hindu University), Varanasi, all rights under copyright that may exist in and for the above thesis submitted for the award of the Doctor of Philosophy.

Date: 11th July 2022

Place: Varanasi



(Mukesh Suthar)

Note: However, the author may reproduce or authorize others to reproduce materials extracted verbatim from the thesis or derivative of the thesis for author's personal use, provided that the source and the Institute's copyright notice are indicated.

ACKNOWLEDGMENT

First and foremost, I would like to thank my supervisor **Dr. Pradip Kumar Roy**, Associate Professor, Department of Ceramic Engineering, Indian Institute of Technology (BHU), Varanasi, for his continuing moral support and inspiring guidance. He has taught me the subject and all aspects of research over the last six years. The freedom he extended to me has helped me grow as an independent researcher. I do not have enough words to express my deep sense of gratitude to him for shaping my career in such a fruitful manner. He will remain forever my friend, philosopher, and guide.

Second, I thank my co-supervisor, **Dr. Shrawan Kr Mishra**, Assistant Professor, School of Material Science & Technology, Indian Institute of Technology (BHU), Varanasi, for his extensive guidance and keen scientific insights through the years.

I am also thankful to my research progress evaluation committee (RPEC) members, **Prof. Sandip Chatterjee** and **Dr. Mohammad Imteyaz Ahmad**, for their kind cooperation during the progression of this work.

I would like to express my sincere thanks to **Prof. V. K. Singh**, HOD, **Prof. Devendra Kumar**, and **Prof. Ram Pyare**, Department of Ceramic Engineering, Indian Institute of Technology (BHU), Varanasi, for extending me necessary administrative support.

I offer my special thanks to **Dr. Ashutosh Kumar Dubey**, **Dr. Indrajit Sinha**, **Dr. N.K. Prasad**, **Dr. Samya Banerjee**, for providing their valuable suggestions & all the necessary facilities for collaborative work.

I would like to offer my special thanks to **Dr. Raj Kumar Joshi** and lab members (especially to **Dr. Avinash Kumar Srivastava**) at MNIT Jaipur for providing all the required facilities to fulfill successful collaborative research.

I would like to extend my sincere thanks to **Professor Rajiv Prakash**, Professor in-charge of the Central Instrument Facility (CIF), Indian Institute of Technology (BHU),

Varanasi, for his support and permission to use the characterization facility. I thank **Mr. Anirban Roy, Mr. Santosh Kumar Patel**, including all technical staff at CIF for the continuous support for the characterization facility. Without their help, I am sure the thesis would not have taken the present shape.

I would like to acknowledge all my friends, lab-mates, and seniors at IIT (BHU), namely **Dr. Deepshikha Shekhawat, Ms. Priyanka Verma, Dr. S. K. Saddam Hossain, Mr. Maurya Sandeep Pradeepkumar, Mr. Deepak Khare, Mr. Anurag Kumar, Ms. Akanksha Gupta, Mr. Satyendra Kumar Singh, Mr. Soham Mukherjee, Mr. P.K. Rao, Ms. Soujanya Madasu, Mr. Sumit Kumar Singh** for their nice company during my stay at the Institute. I thank all my beloved friends across the globe for sharing my happy moments at all times.

Finally, I wish to express my profound thanks to my parents, my elder sisters and brother, and all other family members for their moral support and continuous encouragement while carrying out this study. I also would like to thank my beloved wife **Mohita** and her family for always providing me the moral and unconditional support at each step of my life.

I hope I have not overlooked anyone, but if I have, it is not for lack of appreciation. In case of any omission, I sincerely beg my pardon, and I truly believe that it is purely incidental on my part.



(Mukesh Suthar)

Dedicated
To
My Beloved Parents

Electricity and Magnetism are those forces of nature by which people who know nothing about electricity and magnetism can explain everything.

Egon Friedell

LIST OF CONTENTS

Contents		Page No.
	<i>List of Figures</i>	xiii – xviii
	<i>List of Tables</i>	xix – xxi
	<i>List of Abbreviations</i>	xxii – xxvii
	<i>Preface</i>	xxviii – xxxi
CHAPTER 1	INTRODUCTION	1-22
1.1	Introduction to ferrite	2
1.2	Classification of ferrite	3
1.2.1	Classification based on the magnetic coercivity	4
1.2.1.1	Soft ferrite	4
1.2.1.2	Hard ferrite	4
1.2.2	Classification based on the crystal structure	5
1.2.2.1	Spinel ferrite	5
1.2.2.2	Garnet	6
1.2.2.3	Ortho-ferrite	6
1.2.2.4	Hexaferrite	7
1.3	General properties of ferrite	7
1.4	Applications of ferrite	8
1.5	The structure, composition, and characteristics of hexagonal ferrite	9
1.5.1	Types of hexagonal ferrite	11
1.5.1.1	M-type hexagonal ferrite	12
1.5.1.2	Y-type hexagonal ferrite	13
1.5.1.3	U-type hexagonal ferrite	13
1.5.1.4	W-type hexagonal ferrite	13
1.5.1.5	X-type hexagonal ferrite	13
1.5.1.6	Z-type hexagonal ferrite	14
1.5.2	Applications of hexagonal ferrite materials	14
1.6	The structure, composition, and characteristics of Y-type hexagonal ferrite	15
1.6.1	Cobalt-based Y-type hexagonal ferrite (Co ₂ -Y)	16

1.6.2	Synthesis & properties of Y-type barium hexagonal ferrite (Co ₂ -Y)	18
1.6.3	Explorations of Y-type hexagonal ferrite (Co ₂ -Y)	19
1.7	Theme of the work	21
1.8	Organization of the thesis	21
CHAPTER 2	LITERATURE REVIEW	23-54
2.1	Introduction	24
2.1.1	Substitution at Ba-site in Co ₂ -Y barium hexaferrite	25
2.1.2	Substitution at Co-site in Co ₂ -Y barium hexaferrite	26
2.1.3	Substitution at Fe- Site in Co ₂ -Y barium hexaferrite	26
2.1.4	Substitution at both Ba & Fe- Site in Co ₂ -Y barium hexaferrite	27
2.1.5	Substitution at both Co & Fe- Site in Co ₂ -Y barium hexaferrite	27
2.1.6	Substitution at all three sites (Ba, Co & Fe) in Co ₂ -Y barium hexaferrite	27
2.2	Trends for utilization of ferrite materials in versatile applications	28
2.2.1	Utilization of ferrites as a heterogeneous catalyst for oxidation of styrene	28
2.2.2	Utilization of ferrites as a heterogeneous catalyst for reduction of toxic nitro-organic pollutants	31
2.2.3	Utilization of ferrites as a photocatalyst for treatment of methyl orange contaminated wastewater	35
2.2.4	Utilization of ferrites as a microwave absorber for EMI shielding application	40
2.2.5	Utilization of ferrites as a biocompatible hyperthermia agent	43
2.3	Summary of literature review	51
2.4	Objectives of the work	53
CHAPTER 3	EXPERIMENTAL PROCEDURE	55-82
3.1	Y-type barium hexaferrite synthesis through the sol-gel auto combustion process	56

3.2	Characterization of hexaferrite samples	59
3.2.1	X-ray diffraction analysis	59
3.2.2	Fourier–transform infrared spectroscopy	62
3.2.3	Surface area analysis using BET	64
3.2.4	Nuclear magnetic resonance spectroscopy	65
3.2.5	Scanning electron microscopy (SEM) with EDS analyzer	67
3.2.6	Magnetic property measurement system (MPMS) analysis	69
3.2.7	Magnetothermal analysis	72
3.2.8	Dynamic light scattering analysis	74
3.2.9	UV–Vis Spectroscopy	75
3.2.10	Density measurement	76
3.2.11	X-ray photoelectron spectroscopy	77
3.2.12	Vector network analyzer	79
3.2.13	Fluorescence microscopy	81

RESULTS & DISCUSSION

CHAPTER 4	Cerium substituted Y-type barium hexaferrite (Co₂-Y); as a heterogeneous catalyst for oxidation of styrene	83-106
4.1	Introduction	84
4.2	Results and discussion	85
4.3	Summary	106
CHAPTER 5	Cerium substituted Y-type barium hexaferrite (Co₂-Y); as a heterogeneous catalyst for reduction of toxic nitro-organic pollutants	107-136
5.1	Introduction	108
5.2	Results and discussion	110
5.3	Summary	135
CHAPTER 6	Titanium substituted Y-type barium hexaferrite (Co₂-Y); as a photocatalyst for the treatment of methyl orange contaminated wastewater	137-162
6.1	Introduction	138
6.2	Results and discussion	139

6.3	Summary	161
CHAPTER 7	Lanthanum & magnesium substituted Y-type barium hexaferrite (Co₂-Y); as a microwave absorber for EMI shielding application	163-189
7.1	Introduction	164
7.2	Results and discussion	165
7.3	Summary	189
CHAPTER 8	Chromium substituted Y-type barium hexaferrite (Co₂-Y); as a biocompatible hyperthermia agent	190-209
8.1	Introduction	191
8.2	Results and discussion	194
8.3	Summary	209
CHAPTER 9	CONCLUSIONS AND FUTURE WORK	210-215
9.1	Conclusions	211
9.2	Future scope	215
	References	217-246
	Annexure	247-250
	List of Publications	251-253

LIST OF FIGURES

Figure No.	Content	Page No.
Figure 1.1	Ferrite magnets in different shapes and sizes.	2
Figure 1.2	Globally forecasted growing market trends for the development of ferrite materials.	3
Figure 1.3	Hysteresis loop representation of (a) soft ferrite and (b) hard ferrite.	4
Figure 1.4	Crystal structure representation of normal spinel ferrite.	5
Figure 1.5	Crystal structure representation of garnet ferrite.	6
Figure 1.6	Crystal structure representation of YFeO ₃ ortho-ferrite.	7
Figure 1.7	The general applications of ferrite materials.	9
Figure 1.8	A hexagonal crystal demonstrating lattice parameters a and c.	10
Figure 1.9	The upper section of the ternary phase diagram (Fe ₂ O ₃ -BaO-MeO) presents several hexaferrite phases.	10
Figure 1.10	Schematic representation of basic constituting S, R, and T blocks along with side & oblique view for enhanced visualization.	11
Figure 1.11	The general applications of hexagonal ferrite materials.	14
Figure 1.12	Cross-sectional view of the Ba ₂ Co ₂ Fe ₁₂ O ₂₂ structure where horizontal lines are threefold symmetry axes & the arrows indicates the magnetic moment's orientation of the cations (Fe ³⁺ or Co ²⁺) relative to the <i>c</i> -axis.	16
Figure 3.1	Schematic diagram of the nitrate-based sol-gel auto combustion process.	57
Figure 3.2	Schematic representation of regularly spaced atomic planes and their interaction with incident X-ray radiations.	60
Figure 3.3	Schematic representation of working principle for FTIR spectrometer.	62
Figure 3.4	Schematic representation of working principle for NMR spectrometer	66
Figure 3.5	Schematic representation of working principle for SEM and EDS analyzer.	67
Figure 3.6	Schematic sample assembly representation and a magnified view	69

	of VSM head and SQUID junction.	
Figure 3.7	Schematic representation of magnetothermal analysis equipment.	73
Figure 3.8	Schematic representation of dynamic light scattering-based particle size analyzer.	75
Figure 3.9	Schematic representation of working principle for UV-Visible spectrometer.	76
Figure 3.10	Schematic representation of working principle for X-ray photoelectron spectrometer.	78
Figure 3.11	Block diagram of working principle for vector network analyzer.	80
Figure 3.12	Schematic representation of working principle for fluorescence microscopy.	82
Figure 4.1	(a) XRD patterns of calcined $Ba_{2-x}Ce_xCo_2Fe_{12}O_{22}$ ($x = 0.0, 0.1, 0.2, \& 0.3$) ferrites, (b) Peak shifting of (110) and (1013) peaks.	86
Figure 4.2	FT-IR spectra of calcined $Ba_{2-x}Ce_xCo_2Fe_{12}O_{22}$ ($x = 0.0, 0.1, 0.2, \& 0.3$) ferrite powders.	88
Figure 4.3	SEM, EDX, and Elemental mapping micrographs of calcined pure Y-type barium hexaferrite powder.	89
Figure 4.4	M versus H plot of calcined $Ba_{2-x}Ce_xCo_2Fe_{12}O_{22}$ ($x = 0.0, 0.1, 0.2, \& 0.3$) ferrite powders at room temperature.	90
Figure 4.5	Influence of catalyst amount on the isolated yield for styrene in reaction product (Reaction conditions; Temperature 120°C, Time 24 hrs with TFA).	93
Figure 4.6	Influence of reaction temperature on the isolated yield for styrene in reaction product (Reaction conditions; Catalyst amount 20 mg, Time 24 hrs with TFA).	94
Figure 4.7	Influence of reaction time on the isolated yield for styrene in reaction product (Reaction conditions; Catalyst amount 20 mg, Temp. 120°C with TFA).	95
Figure 4.8	The XPS spectra of $Ba_{1.8}Ce_{0.2}Co_2Fe_{12}O_{22}$ surface (a) wide scan photoelectron spectra with high resolution spectrum corresponding to (b) Ba-3d, (c) Ce-3d, (d) Fe-2p, (e) Co-2p, (f) O-1s regions.	99
Figure 4.9	Plausible reaction mechanism for catalytic oxidation of styrene.	101

Figure 4.10	Reprocess of the catalyst $\text{Ba}_{1.8}\text{Ce}_{0.2}\text{Co}_2\text{Fe}_{12}\text{O}_{22}$ ferrite.	103
Figure 5.1	XRD pattern of calcined $\text{Ba}_2\text{Co}_2\text{Fe}_{12-x}\text{Ce}_x\text{O}_{22}$ ($x = 0.0, 0.1, 0.2, \& 0.3$) ferrite powders.	110
Figure 5.2	FT-IR spectra of calcined $\text{Ba}_2\text{Co}_2\text{Fe}_{12-x}\text{Ce}_x\text{O}_{22}$ ($x = 0.0, 0.1, 0.2, \& 0.3$) ferrite powders.	112
Figure 5.3	Initial magnetization (M versus H) plot of calcined $\text{Ba}_2\text{Co}_2\text{Fe}_{12-x}\text{Ce}_x\text{O}_{22}$ ($x = 0.0, 0.1, 0.2, \& 0.3$) ferrite powders at room temperature.	114
Figure 5.4	Effect of (a) catalyst amount (b) reaction temperature (c) reaction time (d) amount of hydrated hydrazine on reduction of nitrobenzene.	118
Figure 5.5	(a) The wide scan photoelectron spectra of $\text{Ba}_2\text{Co}_2\text{Fe}_{12-x}\text{Ce}_x\text{O}_{22}$ ($x = 0.0, 0.1, 0.2, \& 0.3$) surface, (b) high resolution Ba-3d spectrum.	124
Figure 5.6	The high-resolution spectra of (a) Co-2p and (b) Fe-2p for $\text{Ba}_2\text{Co}_2\text{Fe}_{12-x}\text{Ce}_x\text{O}_{22}$ ($x = 0.0, 0.1, 0.2, \& 0.3$) ferrite samples.	125
Figure 5.7	The high-resolution Ce-3d spectrum for $\text{Ba}_2\text{Co}_2\text{Fe}_{12-x}\text{Ce}_x\text{O}_{22}$ ($x = 0.0, 0.1, 0.2, \& 0.3$) ferrite samples.	126
Figure 5.8	The high-resolution O1s spectrum for $\text{Ba}_2\text{Co}_2\text{Fe}_{12-x}\text{Ce}_x\text{O}_{22}$ ($x = 0.0, 0.1, 0.2, \& 0.3$) ferrite samples.	127
Figure 5.9	Plausible reaction pathway for the reduction of nitrobenzene using $\text{Ba}_2\text{Co}_2\text{Fe}_{11.8}\text{Ce}_{0.2}\text{O}_{22}$ as a heterogeneous catalyst with hydrated hydrazine.	130
Figure 5.10	SEM micrographs of $\text{Ba}_2\text{Co}_2\text{Fe}_{11.8}\text{Ce}_{0.2}\text{O}_{22}$ powder at 10K, 25K, and 50K magnification.	131
Figure 5.11	Reprocess of the $\text{Ba}_2\text{Co}_2\text{Fe}_{11.8}\text{Ce}_{0.2}\text{O}_{22}$ ferrite catalyst.	131
Figure 6.1	XRD patterns of calcined $\text{Ba}_2\text{Co}_2\text{Fe}_{12-x}\text{Ti}_x\text{O}_{22}$ ($x = 0.0, 0.1, 0.2, 0.3, 0.4 \& 0.5$) ferrite powders.	140
Figure 6.2	Williamson–Hall plot for calcined $\text{Ba}_2\text{Co}_2\text{Fe}_{12-x}\text{Ti}_x\text{O}_{22}$ ($x = 0.0, 0.1, 0.2, 0.3, 0.4 \& 0.5$) ferrite powders.	141
Figure 6.3	FT-IR spectra of calcined $\text{Ba}_2\text{Co}_2\text{Fe}_{12-x}\text{Ti}_x\text{O}_{22}$ ($x = 0.0, 0.1, 0.2, 0.3, 0.4 \& 0.5$) ferrite powders.	142
Figure 6.4	DLS analysis for particle size distribution of $\text{Ba}_2\text{Co}_2\text{Fe}_{12-x}\text{Ti}_x\text{O}_{22}$ ($x = 0.0, 0.1, 0.2, 0.3, 0.4 \& 0.5$) ferrite powders.	144

Figure 6.5	Magnetic hysteresis loops of calcined $\text{Ba}_2\text{Co}_2\text{Fe}_{12-x}\text{Ti}_x\text{O}_{22}$ ($x = 0.0, 0.1, 0.2, 0.3, 0.4$ & 0.5) ferrite powders.	145
Figure 6.6	M vs. H^2 plot (Stoner–Wohlfarth model) of calcined $\text{Ba}_2\text{Co}_2\text{Fe}_{12-x}\text{Ti}_x\text{O}_{22}$ ($x = 0.0, 0.1, 0.2, 0.3, 0.4$ & 0.5) ferrite powders.	145
Figure 6.7	Magnetization along and its first order derivative (dM/dT) as a function of temperature (K) for calcined $\text{Ba}_2\text{Co}_2\text{Fe}_{12-x}\text{Ti}_x\text{O}_{22}$ ($x = 0.0, 0.1, 0.2, 0.3, 0.4$ & 0.5) ferrite powders.	146
Figure 6.8	UV-visible diffuse reflectance spectra along with Tauc plot for determination of direct band gap energy of calcined $\text{Ba}_2\text{Co}_2\text{Fe}_{12-x}\text{Ti}_x\text{O}_{22}$ ($x = 0.0, 0.1, 0.2, 0.3, 0.4$ & 0.5) ferrite powders.	150
Figure 6.9	MO degradation in the absence of heterogeneous catalyst using H_2O_2 within (a) dark condition (Fenton) and (b) presence of visible light source (Photo-Fenton).	152
Figure 6.10	MO degradation with $\text{Ba}_2\text{Co}_2\text{Fe}_{12}\text{O}_{22}$ as a heterogeneous catalyst in the presence of H_2O_2 within (a) dark conditions (Fenton) and (b) presence of a visible light source (Photo-Fenton).	152
Figure 6.11	Role of titanium substitution in photocatalytic degradation of MO in the presence of both H_2O_2 and visible light source (Photo-Fenton) with (a) $\text{Ba}_2\text{Co}_2\text{Fe}_{12}\text{O}_{22}$ and (b) $\text{Ba}_2\text{Co}_2\text{Fe}_{11.6}\text{Ti}_{0.4}\text{O}_{22}$	153
Figure 6.12	(a) Comparative analysis of MO degradation with $\text{Ba}_2\text{Co}_2\text{Fe}_{12}\text{O}_{22}$ and $\text{Ba}_2\text{Co}_2\text{Fe}_{11.6}\text{Ti}_{0.4}\text{O}_{22}$ under various controlled conditions (b) Comparison of first-order kinetics ($\ln(C_0/C)$ vs. time plot) of both catalysts.	154
Figure 6.13	SEM micrographs of calcined $\text{Ba}_2\text{Co}_2\text{Fe}_{11.6}\text{Ti}_{0.4}\text{O}_{22}$ hexaferrite powder at two different magnifications of 5K and 20K, along with EDX analysis.	155
Figure 6.14	The XPS analysis of $\text{Ba}_2\text{Co}_2\text{Fe}_{11.6}\text{Ti}_{0.4}\text{O}_{22}$ hexaferrite (a) wide scan XPS survey and high-resolution core spectra of (b) C-1s (c) Ba-3d (d) Co-2p (e) Fe-2p (f) Ti-2p, and (g) O-1s.	156
Figure 6.15	(a) Plausible mechanism for the generation of hydroxyl radicals ($\text{OH}\cdot$) within the Photo-Fenton-based $\text{Co}_2\text{-Y}$ type hexaferrite ferrite/ H_2O_2 system. (b) generation of active hydroxyl radicals ($\text{OH}\cdot$) by relocating electrons within the $\text{Ba}_2\text{Co}_2\text{Fe}_{11.6}\text{Ti}_{0.4}\text{O}_{22}$	158

	hexaferrite system.	
Figure 6.16	Reusability of the $\text{Ba}_2\text{Co}_2\text{Fe}_{11.6}\text{Ti}_{0.4}\text{O}_{22}$ hexaferrite as a catalyst for five consecutive recycling runs under similar conditions.	160
Figure 7.1	XRD patterns of calcined $\text{Ba}_{2-x}\text{La}_x\text{Co}_{2-x}\text{Mg}_x\text{Fe}_{12}\text{O}_{22}$ ($0 \leq x \leq 0.5$) ferrite samples.	166
Figure 7.2	(a) FT-IR spectra, and (b) magnified view of shifting absorption band of calcined $\text{Ba}_{2-x}\text{La}_x\text{Co}_{2-x}\text{Mg}_x\text{Fe}_{12}\text{O}_{22}$ ($0 \leq x \leq 0.5$) ferrite samples.	168
Figure 7.3	SEM micrographs along with EDX spectra of sintered $\text{Ba}_{2-x}\text{La}_x\text{Co}_{2-x}\text{Mg}_x\text{Fe}_{12}\text{O}_{22}$ ($0 \leq x \leq 0.5$) ferrite samples.	171
Figure 7.4	SEM micrograph along with elemental mapping obtained using EDX analysis of $\text{Ba}_{1.5}\text{La}_{0.5}\text{Co}_{1.5}\text{Mg}_{0.5}\text{Fe}_{12}\text{O}_{22}$ ferrite sample.	172
Figure 7.5	Room temperature hysteresis loops of sintered $\text{Ba}_{2-x}\text{La}_x\text{Co}_{2-x}\text{Mg}_x\text{Fe}_{12}\text{O}_{22}$ ($0 \leq x \leq 0.5$) ferrite samples.	173
Figure 7.6	Magnetization vs. $1/H^2$ curves of sintered $\text{Ba}_{2-x}\text{La}_x\text{Co}_{2-x}\text{Mg}_x\text{Fe}_{12}\text{O}_{22}$ ($0 \leq x \leq 0.5$) ferrite samples.	174
Figure 7.7	Thermo-magnetic curves (both FC, ZFC) & first-order derivative of magnetization (the lowermost curve with blue line) of sintered $\text{Ba}_{2-x}\text{La}_x\text{Co}_{2-x}\text{Mg}_x\text{Fe}_{12}\text{O}_{22}$ ($0 \leq x \leq 0.5$) ferrite samples at an applied field of 300 Oe.	179
Figure 7.8	Frequency dependency (a) real and (b) imaginary part of complex permittivity of sintered $\text{Ba}_{2-x}\text{La}_x\text{Co}_{2-x}\text{Mg}_x\text{Fe}_{12}\text{O}_{22}$ ($0 \leq x \leq 0.5$) ferrite samples.	180
Figure 7.9	Frequency dependency (a) real and (b) imaginary part of complex permeability of sintered $\text{Ba}_{2-x}\text{La}_x\text{Co}_{2-x}\text{Mg}_x\text{Fe}_{12}\text{O}_{22}$ ($0 \leq x \leq 0.5$) ferrite samples.	181
Figure 7.10	Frequency dependence of (a) R-parameter (reflectivity) and (b) Ts-parameter (transmissivity) of sintered $\text{Ba}_{2-x}\text{La}_x\text{Co}_{2-x}\text{Mg}_x\text{Fe}_{12}\text{O}_{22}$ ($0 \leq x \leq 0.5$) ferrite samples.	184
Figure 7.11	Frequency dependence (a) SE_R , (b) SE_A , (c) SE_T , (d) attenuation coefficient, (e) σ_{ac} , and (f) R_L of sintered $\text{Ba}_{2-x}\text{La}_x\text{Co}_{2-x}\text{Mg}_x\text{Fe}_{12}\text{O}_{22}$ ($0 \leq x \leq 0.5$) ferrite samples.	187
Figure 8.1	XRD patterns of calcined $\text{Ba}_2\text{Co}_2\text{Fe}_{12-x}\text{Cr}_x\text{O}_{22}$ ($0.0 \leq x \leq 0.5$)	194

	hexaferrite samples.	
Figure 8.2	Williamson–Hall plot for calcined $\text{Ba}_2\text{Co}_2\text{Fe}_{12-x}\text{Cr}_x\text{O}_{22}$ ($0.0 \leq x \leq 0.5$) hexaferrite samples.	195
Figure 8.3	FT-IR spectra of calcined $\text{Ba}_2\text{Co}_2\text{Fe}_{12-x}\text{Cr}_x\text{O}_{22}$ ($0.0 \leq x \leq 0.5$) hexaferrite samples.	196
Figure 8.4	Magnetic hysteresis loops (measured at room temperature) of calcined $\text{Ba}_2\text{Co}_2\text{Fe}_{12-x}\text{Cr}_x\text{O}_{22}$ ($0.0 \leq x \leq 0.5$) hexaferrite samples.	198
Figure 8.5	M vs. H^2 plot (Stoner–Wohlfarth model) of calcined $\text{Ba}_2\text{Co}_2\text{Fe}_{12-x}\text{Cr}_x\text{O}_{22}$ ($0.0 \leq x \leq 0.5$) hexaferrite samples.	199
Figure 8.6	DLS analysis for the particle size distribution of oleic acid-coated $\text{Ba}_2\text{Co}_2\text{Fe}_{12-x}\text{Cr}_x\text{O}_{22}$ ($0.0 \leq x \leq 0.5$) hexaferrite samples.	201
Figure 8.7	(a) The temperature vs. time plots, and (b) variation of SAR and ILP values with chromium concentration for the ferrofluids composed of oleic acid-coated $\text{Ba}_2\text{Co}_2\text{Fe}_{12-x}\text{Cr}_x\text{O}_{22}$ ($0.0 \leq x \leq 0.5$) hexaferrite samples.	203
Figure 8.8	The XPS analysis of $\text{Ba}_2\text{Co}_2\text{Fe}_{11.7}\text{Cr}_{0.3}\text{O}_{22}$ hexaferrite (a) wide scan XPS survey and high-resolution core spectra of (b) C-1s (c) Ba-3d (d) Co-2p (e) Fe-2p (f) Cr-2p, and (g) O-1s.	204
Figure 8.9	SEM micrographs along with EDX spectra of calcined $\text{Ba}_2\text{Co}_2\text{Fe}_{11.7}\text{Cr}_{0.3}\text{O}_{22}$ hexaferrite powder.	206
Figure 8.10	Time and concentration-dependent quantitative analysis (MTT assay) for viability response of pristine (UC) and oleic acid-coated (OC) $\text{Ba}_2\text{Co}_2\text{Fe}_{11.7}\text{Cr}_{0.3}\text{O}_{22}$ hexaferrite powder.	207
Figure 8.11	Fluorescence microscopy images representing the adherence of MG-63 cells after the exposure of the highest studied concentration, i.e., 15 mg/ml (after 72 hrs), within (a) pristine $\text{Ba}_2\text{Co}_2\text{Fe}_{11.7}\text{Cr}_{0.3}\text{O}_{22}$ hexaferrite powder, (b) Oleic acid-coated (OC) $\text{Ba}_2\text{Co}_2\text{Fe}_{11.7}\text{Cr}_{0.3}\text{O}_{22}$ hexaferrite powder, and (c) control.	208

LIST OF TABLES

Table No.	Content	Page No.
Table 1.1	Several types of cobalt-based barium hexaferrite along with their characteristics.	12
Table 1.2	Room temperature magnetic characteristics of Y-type hexaferrites.	15
Table 2.1	Comparative performance of Co ₂ -Y hexaferrite with spinel ferrite materials.	51
Table 4.1	Crystallite size, lattice parameters, <i>c/a</i> ratio, cell volume, surface area, and X-ray density of Ba _{2-x} Ce _x Co ₂ Fe ₁₂ O ₂₂ (x = 0.0, 0.1, 0.2, & 0.3) ferrites.	87
Table 4.2	Wave number, effective mass, force constant, and bond length of Ba _{2-x} Ce _x Co ₂ Fe ₁₂ O ₂₂ (x = 0.0, 0.1, 0.2, & 0.3) ferrites.	88
Table 4.3	Magnetic parameters <i>NB_M</i> , <i>M_s</i> , <i>M_r</i> , <i>M_r/M_s</i> , <i>H_c</i> of Ba _{2-x} Ce _x Co ₂ Fe ₁₂ O ₂₂ (x = 0.0, 0.1, 0.2, & 0.3) ferrites.	91
Table 4.4	Influence of solvent on styrene oxidation.	96
Table 4.5	Influence of oxidizing agent on styrene oxidation.	97
Table 4.6	Performance of as-prepared samples over the oxidation of styrene at optimized conditions.	98
Table 4.7	Substrates scope at optimized conditions for Ba _{1.8} Ce _{0.2} Co ₂ Fe ₁₂ O ₂₂ ferrite.	104
Table 4.8	Confirmation of reaction product obtained with various substrates using ¹ H and ¹³ C NMR spectra.	105
Table 5.1	Crystallite size, lattice parameters, <i>c/a</i> ratio, unit cell volume, X-ray density, surface area, total pore volume and mean pore diameter of calcined Ba ₂ Co ₂ Fe _{12-x} Ce _x O ₂₂ (x = 0.0, 0.1, 0.2, & 0.3) ferrite powders.	111
Table 5.2	Wave number, effective mass, force constant, and bond length of calcined Ba ₂ Co ₂ Fe _{12-x} Ce _x O ₂₂ (x = 0.0, 0.1, 0.2, & 0.3) ferrite powders.	112
Table 5.3	Magnetic parameters <i>NB_M</i> , <i>M_s</i> , <i>M_r</i> , <i>M_r/M_s</i> , <i>H_c</i> , and <i>K_I</i> of calcined Ba ₂ Co ₂ Fe _{12-x} Ce _x O ₂₂ (x = 0.0, 0.1, 0.2, & 0.3) ferrite powders.	113
Table 5.4	Influence of solvent on reduction of nitrobenzene with	121

	Ba ₂ Co ₂ Fe ₁₂ O ₂₂ as a catalyst.	
Table 5.5	Influence of hydrogen source on reduction of nitrobenzene with Ba ₂ Co ₂ Fe ₁₂ O ₂₂ as a catalyst.	122
Table 5.6	Effect of cerium content on the performance of the catalyst in nitro reduction.	123
Table 5.7	Surface ionic ratios of the as-prepared samples using XPS.	128
Table 5.8	Substrates scope for Ba ₂ Co ₂ Fe _{11.8} Ce _{0.2} O ₂₂ ferrite at optimized conditions.	132
Table 5.9	Confirmation of reaction product obtained with various substrates using ¹ H and ¹³ C NMR spectra.	137
Table 6.1	Crystallite size, lattice constants (<i>a</i> & <i>c</i>), (<i>c/a</i>) ratio, unit cell volume, X-ray density and lattice strain of the calcined Ba ₂ Co ₂ Fe _{12-x} Ti _x O ₂₂ (<i>x</i> = 0.0, 0.1, 0.2, 0.3, 0.4 & 0.5) ferrite powders.	141
Table 6.2	Characteristic wave number, effective mass for Fe-O bond, force constant, and corresponding bond length of the calcined Ba ₂ Co ₂ Fe _{12-x} Ti _x O ₂₂ (<i>x</i> = 0.0, 0.1, 0.2, 0.3, 0.4 & 0.5) ferrite powders.	143
Table 6.3	Saturation magnetization (<i>M_s</i>), number of Bohr magneton (<i>N_{BM}</i>), coercivity (<i>H_c</i>), magnetic retentivity (<i>M_r</i>), squareness ratio, magnetic anisotropy constant (<i>K₁</i>), and Curie Temperature (<i>T_c</i>) of the calcined Ba ₂ Co ₂ Fe _{12-x} Ti _x O ₂₂ (<i>x</i> = 0.0, 0.1, 0.2, 0.3, 0.4 & 0.5) ferrite powders.	147
Table 7.1	The unit cell parameters, crystallite size, and X-ray density of the calcined Ba _{2-x} La _x Co _{2-x} Mg _x Fe ₁₂ O ₂₂ (0.0 ≤ <i>x</i> ≤ 0.5) ferrite samples.	167
Table 7.2	Wave number, effective mass, force constant, and bond length of the calcined Ba _{2-x} La _x Co _{2-x} Mg _x Fe ₁₂ O ₂₂ (0.0 ≤ <i>x</i> ≤ 0.5) ferrite samples.	169
Table 7.3	Values of bulk density, percentage porosity, and grain size of the sintered Ba _{2-x} La _x Co _{2-x} Mg _x Fe ₁₂ O ₂₂ (0.0 ≤ <i>x</i> ≤ 0.5) ferrite samples.	170
Table 7.4	The saturation magnetization (<i>M_s</i>), remnant magnetization (<i>M_r</i>), number of Bohr magneton (<i>N_{BM}</i>), squareness ratio (<i>M_r/M_s</i>), coercivity (<i>H_c</i>), anisotropy field (<i>H_a</i>), and magnetic anisotropy constant (<i>K₁</i>) of the sintered Ba _{2-x} La _x Co _{2-x} Mg _x Fe ₁₂ O ₂₂ (0.0 ≤ <i>x</i> ≤	175

	0.5) ferrite samples.	
Table 7.5	Values of electromagnetic and shielding parameters of the sintered $\text{Ba}_{2-x}\text{La}_x\text{Co}_{2-x}\text{Mg}_x\text{Fe}_{12}\text{O}_{22}$ ($0.0 \leq x \leq 0.5$) ferrite samples at different frequencies.	186
Table 8.1	The crystallite size, lattice constants (a & c), axial ratio, unit cell volume, X-ray density and lattice strain of the calcined $\text{Ba}_2\text{Co}_2\text{Fe}_{12-x}\text{Cr}_x\text{O}_{22}$ ($0.0 \leq x \leq 0.5$) hexaferrites.	195
Table 8.2	Characteristic wave number, effective mass, force constant, and corresponding bond length for Fe-O bond of the calcined $\text{Ba}_2\text{Co}_2\text{Fe}_{12-x}\text{Cr}_x\text{O}_{22}$ ($0.0 \leq x \leq 0.5$) hexaferrites.	197
Table 8.3	The saturation magnetization (M_s), magnetic retentivity (M_r), coercivity (H_c), Bohr magneton (N_{BM}), squareness ratio (S_R), magnetic anisotropy constant (K_I), and effective magnetocrystalline anisotropy constant (K_{eff}) of the calcined $\text{Ba}_2\text{Co}_2\text{Fe}_{12-x}\text{Cr}_x\text{O}_{22}$ ($0.0 \leq x \leq 0.5$) hexaferrite samples.	200
Table 8.4	The mean particle size, poly-dispersion index (PDI), initial heating rate (dT/dt), specific absorption rate (SAR), and intrinsic loss power (ILP) of oleic acid-coated $\text{Ba}_2\text{Co}_2\text{Fe}_{12-x}\text{Cr}_x\text{O}_{22}$ ($0.0 \leq x \leq 0.5$) hexaferrite samples.	202

LIST OF ABBREVIATIONS AND SYMBOLS

Co ₂ -Y	Cobalt based Y-type barium hexaferrite
EMI	Electromagnetic interference
UHF	Ultrahigh-frequency
emu	Electromagnetic unit
NB	Nitrobenzene
UV	Ultraviolet
min	Minutes
MO	Methyl orange
mM	Millimolar
mg	Milligram
MB	Methyl blue
DB122	Direct black 122
GHz	Gigahertz
FMR	Ferromagnetic resonance
GPS	Global positioning system
DNA	Deoxyribonucleic acid
MHz	Megahertz
NPR	Novolac phenolic resin
dB	Decibel
MRI	Magnetic resonance imaging
SLP	Specific loss power
SAR	Specific absorption rate
AC	Alternating current
ILP	Intrinsic loss power
LRT	linear response theory
SLP	Specific loss power
kHz	Kilohertz
CFO	Cobalt ferrite
HA	Hydroxyapatite
GR	General reagent
DGG	Discontinuous grain growth

M	Molar mass
hrs	Hours
PVA	Polyvinyl alcohol
mm	Millimeter
MPa	Megapascal
XRD	X-ray diffraction
IR	Infrared
FTIR	Fourier-transform infrared spectroscopy
cm	Centimetre
ATR	Attenuated total reflection
STP	Standard temperature and pressure
nm	Nanometer
NMR	Nuclear magnetic resonance
SEM	Scanning electron microscopy
SE	Secondary electrons
BSE	Back-scattered electrons
EDS	Energy-dispersive X-ray spectroscopy
DC	Direct current
VSM	Vibrating sample mode
SQUID	Superconducting Quantum Interference Device
QLS	Quasi-elastic light scattering
PCS	Photon correlation spectroscopy
DLS	Dynamic light scattering
PDI	Poly-dispersion index
XPS	X-ray photoelectron spectroscopy
μm	Micrometer,
VNA	Vector network analyzer
SWR	Standing wave ratio
DUT	Device under test
TFA	Trifluoroacetic acid
TLC	Thin-layer chromatography
NMR	Nuclear magnetic resonance
JCPDS	Joint committee on powder diffraction standards

M _w	Molecular weight
mL	Milliliters
MeOH	Methanol
PTSA	p-Toluenesulfonic acid
eV	Electron volt
NO	Nitrogen monoxide
CO	Carbon monoxide
mmol	Millimole
DMF	Dimethylformamide
IPA	Isopropyl alcohol
EtOH	Ethanol
BE	Binding energy
ppm	Parts per million
DI water	Deionized water
NCCS	National center for cell science
DMEM	Dulbecco's modified eagle medium
FBS	Fetal bovine serum
RH	Relative humidity
EDTA	Ethylenediaminetetraacetic acid
mT	Millitesla
UC	Un-coated
OC	Oleic acid-coated
OD	Optical density
CI	Confidence interval
T _{sp}	Spin transition temperature
T _c	Curie temperatures.
M _s	Saturation magnetization
H _c	Coercivity
M _r	Magnetic retentivity
S _R	Squareness ratio
K ₁	Magnetic anisotropy constant
λ	Wavelength
θ	Bragg's angle

d	Inter-planer spacing
n	Diffraction order
k_s	Sherrer's constant
D_m	Crystallite size
W_{hkl}	Full width at half maxima
$W_{hkl}^{measured}$	Full width at half maxima of measured peak
$W_{hkl}^{instrumental}$	Instrumental broadening
a and c	Lattice parameters
$h\ k\ l$	Miller index
V_{uc}	Unit cell volume
D_x	X-ray density
Z_e	Effective number of formula units
N_a	Avogadro's constant
ϵ	Lattice strain
L_b	Bond length
F	Force constant
\AA	Angstrom
ν_{wn}	Wavenumber
c_{vl}	Speed of light
μ_{em}	Effective mass of bonded atoms
M_1 and M_2	Atomic weights of bonded atoms
P_g	Gas pressure
θ_{fs}	Surface area with monolayer adsorption
X	Weight of adsorbed nitrogen at a relative pressure of (P/P_o)
X_m	Volume required to achieve monolayer adsorption of gas at STP
S_a	Sample surface area
A_m	Cross-sectional area
M_v	Molar volume
^1H	Proton
K	Kelvin
H	Magnetic field
χ	Susceptibility at higher field
H_a	Anisotropy field

μ_0	Free space permeability
f	Frequency
W	Watt
C_d	Specific heat capacity of the dispersant
M_{np}	Mass of magnetic nanoparticles
H_{AC}	AC magnetic field strength
I_0	Initial intensity of light and
I	Outgoing intensity through the sample
C_M	Molar concentration of material within the solvent
P_L	Path length through which the radiation has to interact with the sample
ϵ_{MA}	Molar absorptivity of that material
D_{Bulk}	Bulk density
$P\%$	Percentage porosity
W_D	Dry weight
W_S	Soaked weight
W_A	Suspended weight
$E_{binding}$	Energy of an electron attached to the nucleus,
E_{photon}	Energy of the X-ray photons dependent on the X-ray source
$E_{kinetic}$	Kinetic energy of the emitted electron
Δ	Work function
$S_{21}, S_{12}, S_{11}, S_{22}$	Scattering parameters
χ''	Imaginary part of susceptibility
ρ_m	Mass density
P_d^{LRT}	Power dissipation from linear response theory
χ_0	Susceptibility value at equilibrium
τ	Neel-Brown relaxation time
k_B	Boltzmann constant
V_p	Volume of particle
V_{opt}	Optimum volume
DMF	Dimethylformamide
T	Tesla
ZFC	Zero-field-cooled

FC	Field-cooled
α	Coefficient of absorption
ν	Incident photon frequency
K_T	Energy-independent constant
K_{arc}	Apparent rate constant or pseudo-first-order rate constant
C_o	Initial concentration
N	Newtons
$(\epsilon = \epsilon' - i\epsilon'')$	Complex permittivity
$(\mu = \mu' - i\mu'')$	Complex permeability
ζ	Extinction coefficient,
R_L	Reflection loss
SE_T	Total shielding effectiveness
SE_A	Shielding effectiveness due to absorption
SE_R	Shielding effectiveness due to reflection
SE_M	Shielding effectiveness due to multiple reflective
P_T	Power transmitted
P_I	Power incident
T_s	Transmissivity of incident radiation
R	Reflectivity of incident radiation
ξ	Attenuation coefficient
σ_{ac}	AC conductivity
S	Siemens
ϵ_o	Permittivity of vacuum
<i>PBS</i>	Phosphate buffered saline
K_{eff}	Effective magnetocrystalline anisotropy constant

ABSTRACT

The hexaferrites, which occupy a major class of oxides with significant magnetic properties, have been investigated and applied during the last 60 years. The applications of these materials encompass an impressive range extending from millimeter-wave integrated circuitry to intricate power handling transformers, simple permanent magnets to sophisticated reading heads, and many other remarkable technical involvements. Although all these applications belong to the basic properties of ferrites, a vast level of research has begun concentrating on tuning these basic parameters through elemental manipulations.

The Y-type hexaferrite ($\text{Co}_2\text{-Y}$), having the chemical formula ($\text{Ba}_2\text{Co}_2\text{Fe}_{12}\text{O}_{22}$), is a magnetoelectric multiferroic (type II) material. It has planar magnetic anisotropy at room temperature and is made up of alternating stacking of T ($\text{Ba}_2\text{Fe}_8\text{O}_{14}$) and S ($\text{Co}_2\text{Fe}_4\text{O}_8$) blocks with a corresponding rotation of 120° along the c -axis after each TS pair. The S block is responsible for the net magnetic moment for this ferrite system along the direction of Fe^{3+} ions from the octahedral site. In contrast, the magnetic moments of the T block cancel out the contribution arising from the octahedral and tetrahedral site ions. The inherent properties such as better thermochemical stability, excellent mechanical hardness, wear and corrosion resistance, and higher value of Curie temperature associated with $\text{Co}_2\text{-Y}$ hexaferrite may facilitate the adoption of this material to be utilized within the diverse field of applications.

The present research work includes several aspects of achieving a successful tunability of the concerned compound, i.e., Y-type barium hexaferrite ($\text{Co}_2\text{-Y}$), to overcome the flaws associated with earlier studied ferrite (especially spinel-type) systems within its real-time adoption by the industries. The thesis deals with exploring the

performance of substituted $\text{Co}_2\text{-Y}$ hexaferrite, synthesized using the citrate-nitrate auto-combustion method, within five versatile fields, including i) heterogeneous catalysis for oxidation (conversion of styrene to benzaldehyde), ii) heterogeneous catalysis for reduction or hydrogenation (conversion of nitrobenzene compound to aniline), iii) heterogeneous photocatalysis for wastewater treatment (degradation of aqueous methyl orange), iv) as a microwave absorbing material for EMI shielding application and v) as a biocompatible hyperthermia agent.

The cerium substituted nanocrystalline Y-type barium hexaferrite $\{\text{Ba}_{2-x}\text{Ce}_x\text{Co}_2\text{Fe}_{12}\text{O}_{22}$ ($x = 0.0, 0.1, 0.2, \& 0.3$) $\}$ can be selected as an industrially adoptable heterogeneous catalyst for the conversion of styrene to benzaldehyde. The as-prepared hexaferrite shows excellent catalytic performance due to its high surface area and large dispersity by providing additional active sites for the reaction. The optimum catalytic efficiency has been achieved by using 20 mg of $\text{Ba}_{1.8}\text{Ce}_{0.2}\text{Co}_2\text{Fe}_{12}\text{O}_{22}$ hexaferrite at a reaction temperature of 120°C for 24 hrs with trifluoroacetic acid (TFA) as an oxidant. It results in the 71% isolated yield for the concerned product (benzaldehyde) with a total consumption of styrene. The as-prepared catalyst is magnetically separable to reprocess. There is no remarkable loss of catalytic activity when it is reprocessed for five consecutive trials.

The cerium substituted nanocrystalline Y-type barium hexaferrite $\{\text{Ba}_2\text{Co}_2\text{Fe}_{12-x}\text{Ce}_x\text{O}_{22}$ ($x = 0.0, 0.1, 0.2, \& 0.3$) $\}$ can be designed as an industrially adoptable heterogeneous catalyst for the conversion of nitrobenzene to aniline. The as-prepared ferrite powder can be utilized in a large-scale wastewater treatment plant or industrial conversion of aromatic nitro compounds to the corresponding amine. The optimum catalytic efficiency has been attained by using 100 mg of $\text{Ba}_2\text{Co}_2\text{Fe}_{11.80}\text{Ce}_{0.20}\text{O}_{22}$ hexaferrite at a reaction temperature of 100°C for 12 hrs with 2 mmol of hydrated

hydrazine within the water as a solvent. It results in the 73% isolated yield for the concerned product (aniline) with a total consumption of nitrobenzene.

The Ti-substituted nanocrystalline Y-type barium hexaferrite $\text{Ba}_2\text{Co}_2\text{Fe}_{12-x}\text{Ti}_x\text{O}_{22}$ ($x = 0.0, 0.1, 0.2, 0.3, 0.4$ & 0.5) can be explored as a heterogeneous photocatalyst for the degradation of methyl orange from the wastewater. The UV-visible spectrum analysis supports the enhancement in visible light absorption and decreasing behavior for bandgap value by increasing the substitution level of Ti^{4+} ions within the sample. The photocatalytic degradation study of aqueous MO solution in the presence of H_2O_2 suggests the superiority of $\text{Ba}_2\text{Co}_2\text{Fe}_{11.6}\text{Ti}_{0.4}\text{O}_{22}$ compared to pristine Co_2 -Y barium hexaferrite with an apparent rate constant of $1.9 \times 10^{-2} \text{ min}^{-1}$ and turn over frequency of $3.93 \times 10^{-6} \text{ mole g}^{-1}\text{min}^{-1}$. This enhanced photocatalytic activity for sample $\text{Ba}_2\text{Co}_2\text{Fe}_{11.6}\text{Ti}_{0.4}\text{O}_{22}$ can be correlated to the fine crystallite size; the presence of active Ti^{3+} species to promote the reactivity of catalyst surface; the presence of mixed Fe^{3+} & Fe^{2+} to slow down the recombination process by trapping the photogenerated electrons and holes; the existence of oxygen vacancy to enhance the visible light absorption and leads to narrowing the bandgap by creating an extra impurity level adjacent to the valence band.

The lanthanum and magnesium substituted nanocrystalline Y-type barium hexaferrite $\text{Ba}_{2-x}\text{La}_x\text{Co}_{2-x}\text{Mg}_x\text{Fe}_{12}\text{O}_{22}$ ($x = 0.0, 0.1, 0.2, 0.3, 0.4$ & 0.5) can be employed as a microwave absorbing material for EMI shielding applications. The magnetic measurements reveal that the saturation magnetization decreases, and the coercivity increases with increasing La^{3+} and Mg^{2+} content. The optimum EMI shielding and microwave absorbance performance have been achieved by $\text{Ba}_{1.5}\text{La}_{0.5}\text{Co}_{1.5}\text{Mg}_{0.5}\text{Fe}_{12}\text{O}_{22}$ composition at a thickness of 5 mm with a moderate value of reflection loss ($R_L < -10\text{dB}$), resulting in 90% absorption of the incident microwave.

The chromium substituted cobalt-based nanocrystalline Y-type barium hexaferrite $\text{Ba}_2\text{Co}_2\text{Fe}_{12-x}\text{Cr}_x\text{O}_{22}$ ($x = 0.0, 0.1, 0.2, 0.3, 0.4$ & 0.5) can be applied as a biocompatible hyperthermia agent. The surface of the ferrite particles is functionalized using oleic acid to overcome the issue associated with ferrofluid stability and analyzed their biocompatibility using the MG-63 cell line. The optimum hyperthermic performance is accomplished by $\text{Ba}_2\text{Co}_2\text{Fe}_{11.7}\text{Cr}_{0.3}\text{O}_{22}$ ferrite under an applied AC magnetic field of 25 mT at a frequency of 114.1 kHz, resulting in the SAR value of 84.39 W/g and ILP value of $1.86 \text{ nHm}^2/\text{Kg}$ with excellent biocompatibility.

The enhanced performance of all these substituted $\text{Co}_2\text{-Y}$ hexaferrite samples has been explained by the variations in structural, magnetic, morphological parameters and the presence of multivalence elemental states within the samples. This work indicates that the catalytic oxidation, catalytic reduction, photocatalytic degradation, microwave absorptivity, and the magnetic hyperthermia activity of the complex ferrites are not only limited to conventionally utilized soft ferrite materials but also can be explored to hard ferrites too. The substituted Y-type barium hexaferrite ($\text{Co}_2\text{-Y}$) proves its promising candidacy with several advantages such as ease of separation, better reusability, excellent thermochemical stability, total conversion of reactant, better selectivity for the desired product, lower value of band gap energy, total degradation of non-biodegradable dye, the optimum value of EMI shielding and microwave absorption, exceptional heating capability within AC magnetic field and excellent biocompatibility.

Keywords: *Y-type barium hexaferrite; Sol-gel auto combustion; Heterogeneous catalyst; Oxidation; Reduction; Photocatalyst; Microwave absorption; Magnetic hyperthermia*